Electronic supplementary information (ESI) for

Iron Phosphate Nanoparticle Catalyst for Direct Oxidation of Methane into Formaldehyde: Effect of Surface Redox and Acid-Base Properties

*Aoi Matsuda,[a] Haruka Tateno,[a] Keigo Kamata,[*abc] and Michikazu Hara[*a]*

[a] Laboratory for Materials and Structures, Institute of Innovative Research, Tokyo Institute of Technology, 4259 Nagatsuta-cho, Midori-ku, Yokohama, Kanagawa 226-8503, Japan

[b] Japan Science and Technology Agency (JST), Precursory Research for Embryonic Science and Technology (PRESTO), 4-1-8 Honcho, Kawaguchi, Saitama 332-0012, Japan

[c] JST, Core Research for Evolutional Science and Technology (CREST), 4-1-8 Honcho, Kawaguchi, Saitama 332-0012, Japan

E-mail: kamata.k.ac@m.titech.ac.jp, hara.m.ae@m.titech.ac.jp

Experimental

Materials. Reagents such as $Fe(NO_3)_3 \cdot 9H_2O$, $Fe(OAc)_2$, $NH_4H_2PO_4$, DL-malic acid, and L-aspartic acid were purchased from Kanto Chemical and used as-received. Distilled water was produced in-house using a water purifier (Yamato Auto Still WG202). Helium ($\geq$99.99995%), methane ($\geq$99.999%), oxygen ($\geq$99.99995%), and nitrogen ($\geq$99.99995%) were used as-received for the catalytic oxidation of methane.

Instruments. Bulk properties of solid materials were investigated by the following procedures.[S1–S5] Samples were identified by X-ray diffraction (XRD) using a diffractometer (MiniFlex, Rigaku) with Cu Kα radiation (λ = 1.5405 Å, 40 kV–15 mA)

and equipped with a high-speed 1-dimensional detector (D/teX Ultra).   Data were collected in the 2θ range of 10–80° in 0.02° steps with a continuous scanning rate of 20° min^{-1}.   The chemical composition was analyzed using inductively coupled plasma-atomic emission spectroscopy (ICP–AES; ICPS-8100, Shimadzu).   Diffuse reflectance infrared Fourier transform spectra were obtained using a spectrometer (FT/IR-6100, JASCO) equipped with a diffuse reflectance attachment.

Thermogravimetry-differential thermal analysis (TG-DTA) was performed using a differential thermal analyzer (DTG-60, Shimadzu), and the measurements were conducted under both reductive and oxidative conditions.   First, the atmosphere of the furnace was replaced with H_2/N_2 by pretreating the sample in a H_2/N_2 (20/180 mL min^{-1}) flow at room temperature for 30 min prior to the measurement, and the temperature was increased from room temperature to 650 °C at a heating rate of 5 °C min^{-1} and held for 30 min in a H_2/N_2 (20/180 mL min^{-1}) flow.   After cooling to room temperature, the gas flow was changed to O_2 (200 mL min^{-1}) and held for 30 min.   The atmosphere of the furnace was then replaced with O_2 by pretreating the sample in a O_2 (200 mL min^{-1}) flow at room temperature for 30 min prior to the measurement, after which the temperature was increased from room temperature to 650 °C at a heating rate of 5 °C min^{-1} and held for 30 min in an O_2 (200 mL min^{-1}) flow.

H_2 temperature-programmed reduction (H_2-TPR) profiles were measured on a chemisorption analyzer (BELCAT-A, BEL Japan) equipped with a thermal conductivity detector (TCD) to measure changes in the decrease of H_2 in the gas stream.   50 mg of sample was placed in a quartz cell and then heated from 50 to 700 °C at a rate of 5 °C min^{-1} under 5% H_2/Ar flow (50 mL min^{-1}).

The surface properties of the solid materials were investigated by the following procedures.[S1–S5]   The specific surface area was determined by nitrogen adsorption-desorption isotherms measured at −196 °C with an automatic surface area and porosimetry analyzer (Tristar II, Micromeritics), and the Brunauer-Emmett-Teller (BET) surface area was estimated over the relative pressure (P/P_0) range of 0.05–0.30.   The sample was heated at 150 °C for 2 h under vacuum prior to the measurements, and the BET method was utilized to calculate the specific surface area.   The morphology was characterized using scanning electron microscopy (SEM; S-4800, Hitachi).   After directly mixing Cu grids with samples, the Cu grids were collected and mounted on a stage.   X-ray photoelectron spectroscopy (XPS) data were collected on a spectrometer (ESCA-3400HSE, Shimadzu) with a standard Mg Kα source (1253.6 eV) operated at 10

kV and 25 mA.　Samples were pressed into pellets and fixed on a piece of double-sided carbon tape.　The binding energy was calibrated assuming the binding energy of the C 1s line to be 284.6 eV.

Procedure for IR measurements.　The amounts of Lewis and Bronsted acid sites on FePO$_4$-MA and Fe$_2$O$_3$ catalysts were estimated from FT-IR measurements for pyridine-adsorbed samples at 25 °C.[S5–S7]　Samples were pressed into self-supporting disks (20 mm diameter, 17.8 mg and 78.6 mg for FePO$_4$-MA and Fe$_2$O$_3$, respectively) and placed in an IR cell attached to a closed glass-circulation system.　Prior to pyridine adsorption, the sample was dehydrated by heating at 300 °C for 1 h under vacuum.　The intensity of the band at 1450 cm^{-1} (pyridine coordinatively bonded to Lewis acid sites, molecular absorption coefficient: 4.5 and 1.8 cm$^2\cdot\mu$mol^{-1} for FePO$_4$-MA and Fe$_2$O$_3$, respectively) was plotted against the amount of pyridine adsorbed on the Lewis acid sites of the samples. The band intensity increased with the amount of chemisorbed pyridine and reached a plateau with the appearance of the band due to physisorbed pyridine (ca. 1440 cm^{-1}). While the band around 1440 cm^{-1} disappeared after evacuation at room temperature for 4 h, there was no significant difference in the intensity of the 1446 cm^{-1} band before and after evacuation, which indicated that the maximum intensity of the 1446 cm^{-1} band corresponded to the amount of Lewis acid sites available to chemisorb pyridine until saturation.　The amounts of Lewis acid sites on FePO$_4$-MA and Fe$_2$O$_3$ were estimated to be 13 and 50 μmol g^{-1}, respectively, from the maximum band intensities and molecular absorption coefficient at 1446 cm^{-1}.　The relationship among the surface Lewis acid sites, surface active sites, and CH$_4$ oxidation performance is discussed in "3.1 Synthesis and characterization of iron-based catalysts" and "3.4 Acid-base properties of iron-based catalysts".　For IR measurements with chloroform-adsorbed samples at 25 °C, a dehydrated sample (by heating at 300 °C for 1 h under vacuum) was exposed to chloroform vapor, and Fig. 10(a) shows IR spectra for FePO$_4$-MA and Fe$_2$O$_3$ at gas-phase chloroform pressures of 2.7×10^{-2} and 1.4×10^{-2} kPa, respectively. IR measurements with acetone and methanol-adsorbed samples at 25 °C were prepared by exposure of the dehydrated sample (by heating at 300 °C for 1 h under vacuum) to saturated acetone and methanol vapor followed by evacuation at 25 °C for 30 min to remove weakly physisorbed acetone and methanol.
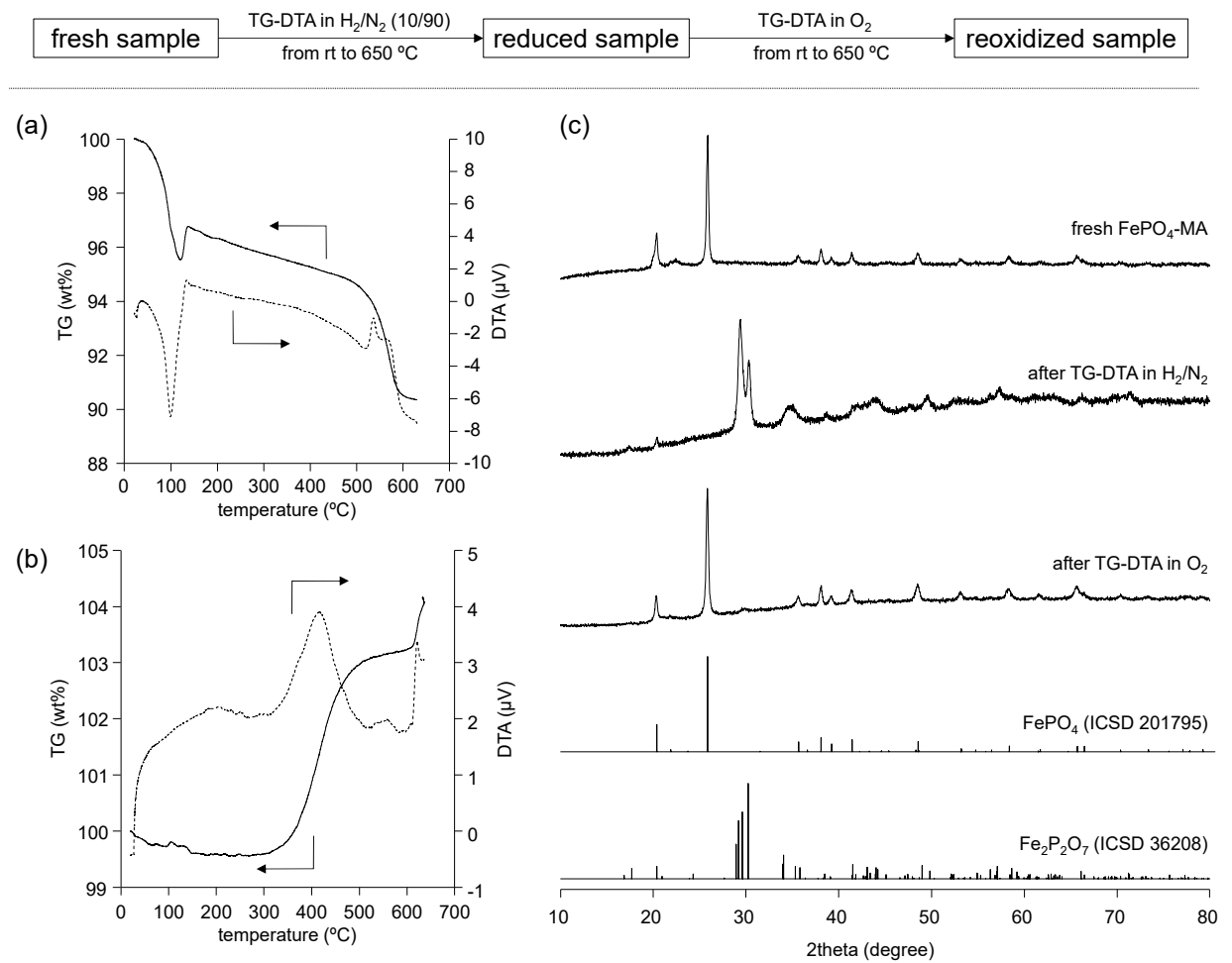
Fig. S1 TG-DTA profiles for (a) fresh FePO$_4$-MA in H$_2$/N$_2$ (10/90, v/v) and (b) reduced FePO$_4$-MA in O$_2$. (c) XRD patterns for fresh FePO$_4$-MA, reduced FePO$_4$-MA, reoxidized FePO$_4$-MA, FePO$_4$ (ICSD 201795), and Fe$_2$P$_2$O$_7$ (ICSD 36208).
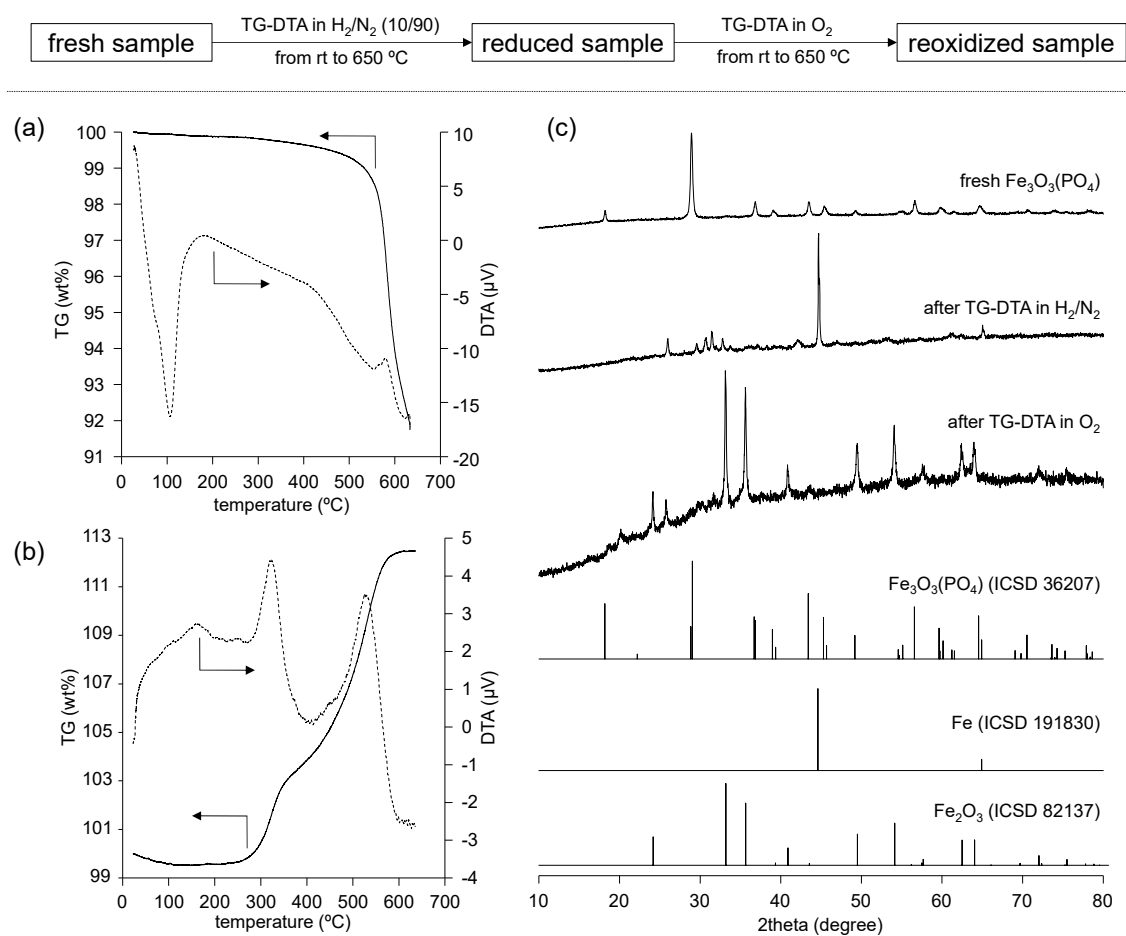
Fig. S2 TG-DTA profiles for (a) fresh $Fe_3O_3(PO_4)$ in H_2/N_2 (10/90, v/v) and (b) reduced $Fe_3O_3(PO_4)$ in O_2. (c) XRD patterns for fresh $Fe_3O_3(PO_4)$, reduced $Fe_3O_3(PO_4)$, reoxidized $Fe_3O_3(PO_4)$, $Fe_3O_3(PO_4)$ (ICSD 36207), Fe (ICSD 191830), and Fe_2O_3 (ICSD 82137).
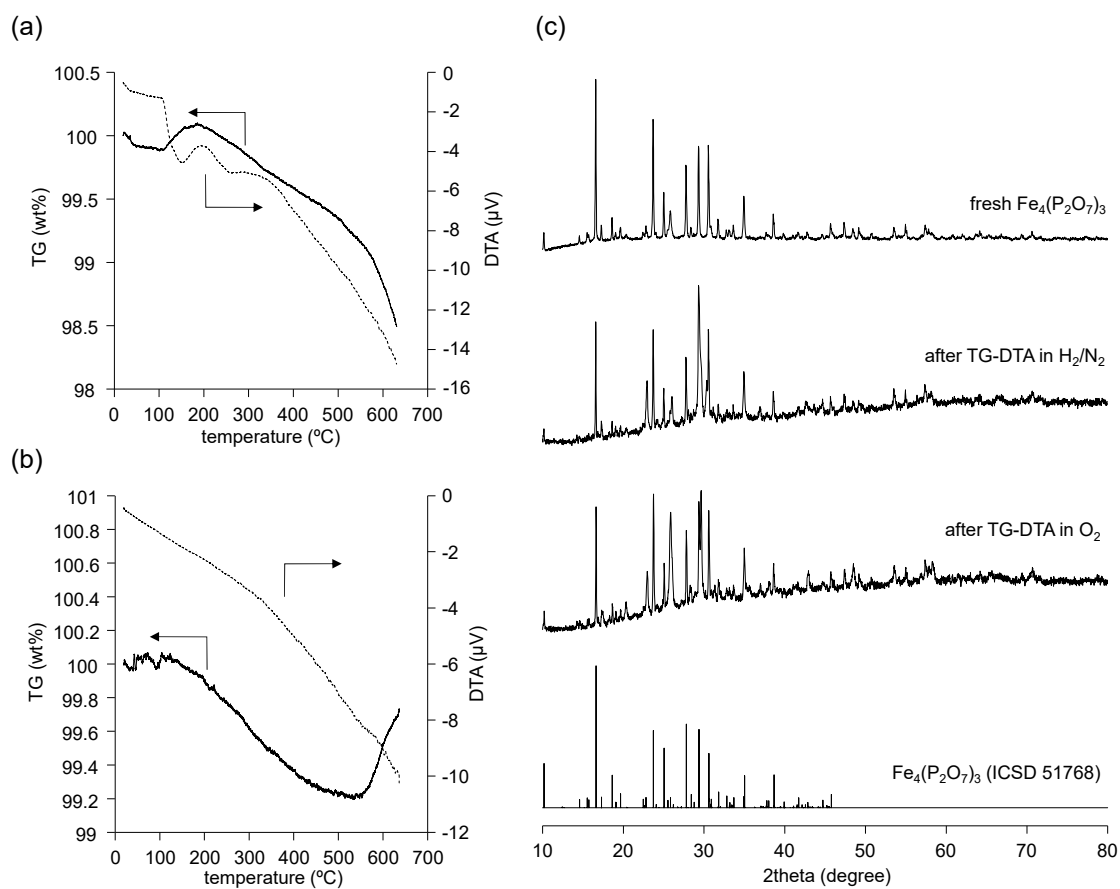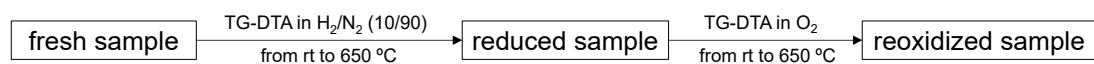
Fig. S3 TG-DTA profiles for (a) fresh $Fe_4(P_2O_7)_3$ in H_2/N_2 (10/90, v/v) and (b) reduced $Fe_4(P_2O_7)_3$ in O_2.   (c) XRD patterns for fresh $Fe_4(P_2O_7)_3$, reduced $Fe_4(P_2O_7)_3$, reoxidized $Fe_4(P_2O_7)_3$, and $Fe_4(P_2O_7)_3$ (ICSD 51768).

S6
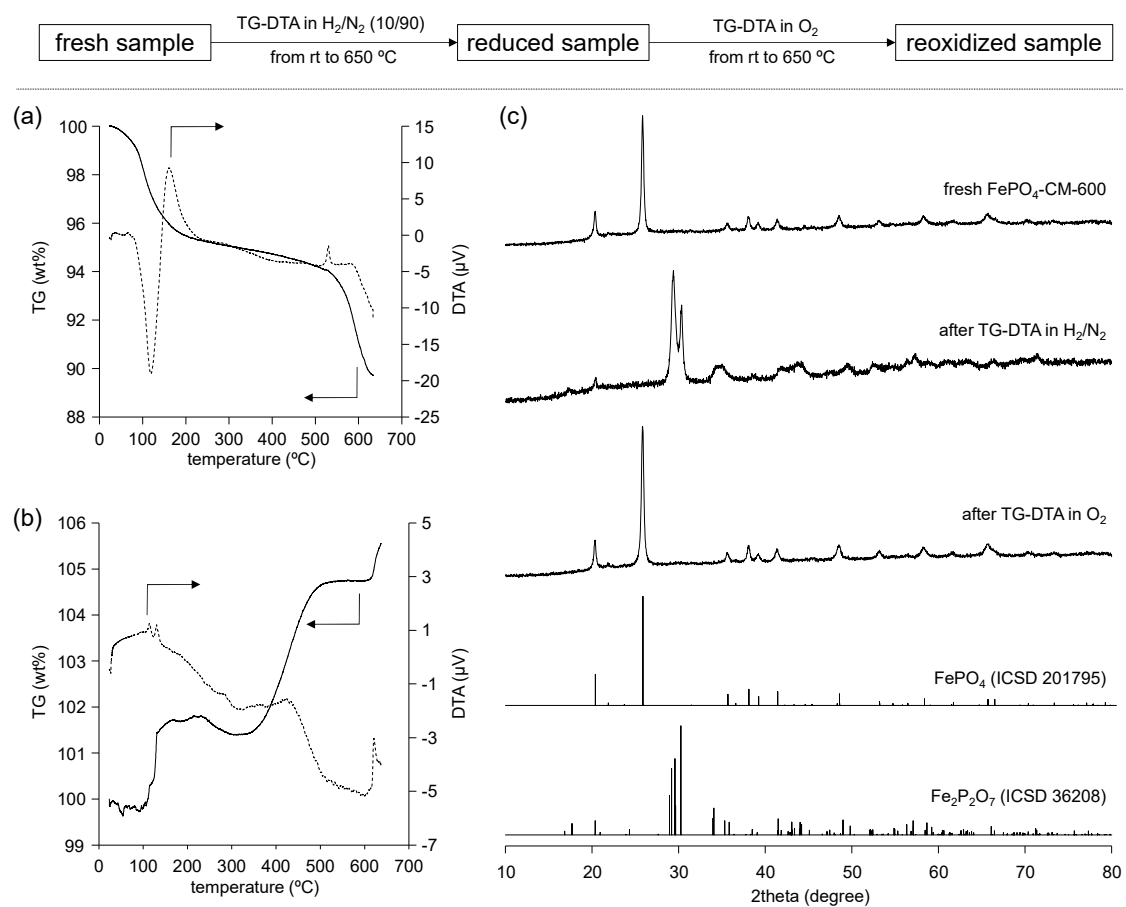
Fig. S4 TG-DTA profiles for (a) fresh FePO$_4$-CM-600 in H$_2$/N$_2$ (10/90, v/v) and (b) reduced FePO$_4$-CM-600 in O$_2$. (c) XRD patterns for fresh FePO$_4$-CM-600, reduced FePO$_4$-CM-600, reoxidized FePO$_4$-CM-600, FePO$_4$ (ICSD 201795), and Fe$_2$P$_2$O$_7$ (ICSD 36208).
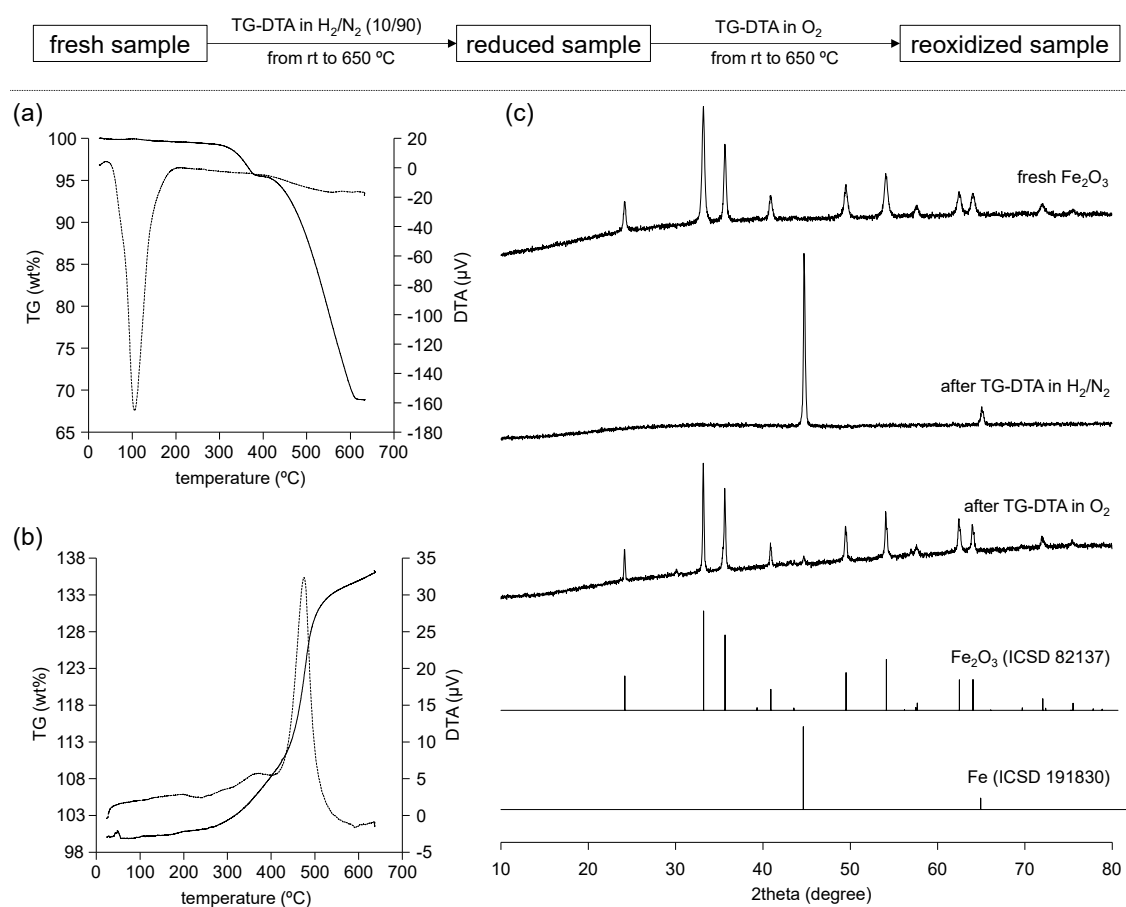
Fig. S5 TG-DTA profiles for (a) fresh Fe_2O_3 in H_2/N_2 (10/90, v/v) and (b) reduced Fe_2O_3 in O_2. (c) XRD patterns for fresh Fe_2O_3, reduced Fe_2O_3, reoxidized Fe_2O_3, Fe_2O_3 (ICSD 82137), and Fe (ICSD 191830).
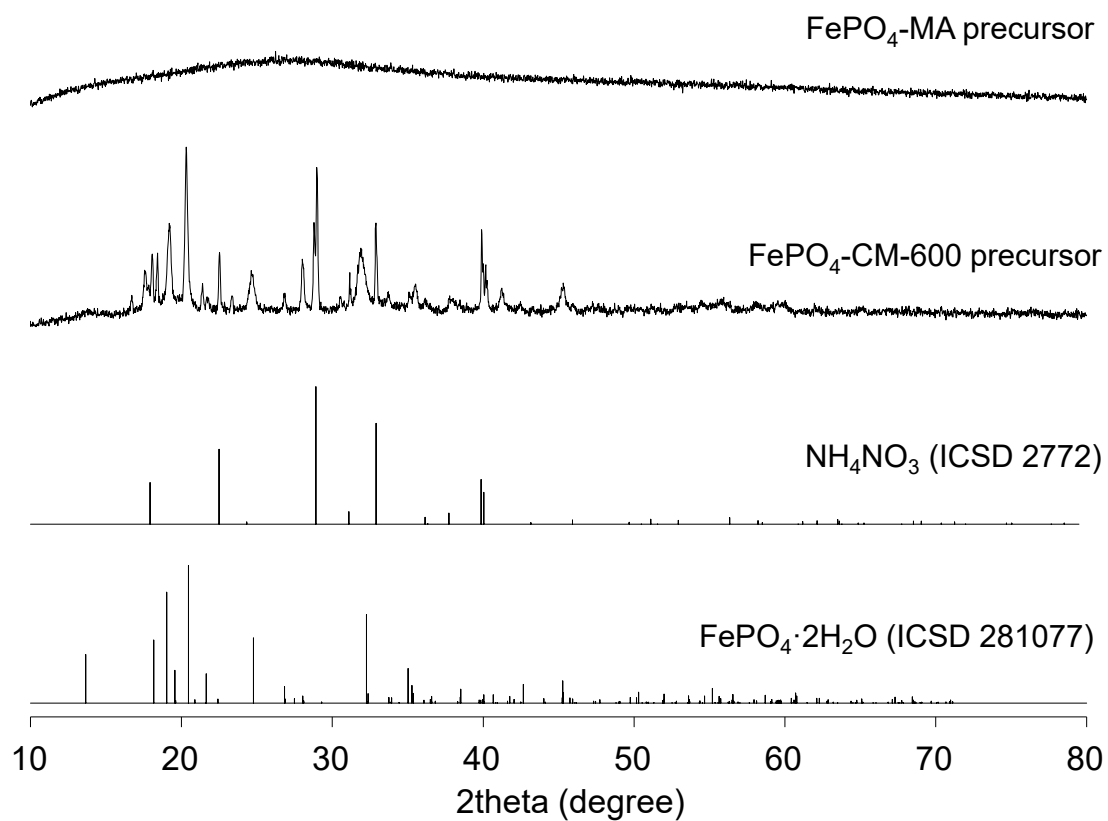
Fig. S6 XRD patterns for the precursors of FePO4-MA and FePO4-CM-600, NH4NO3 (ICSD 2772), and FePO4·2H2O (ICSD 281077).
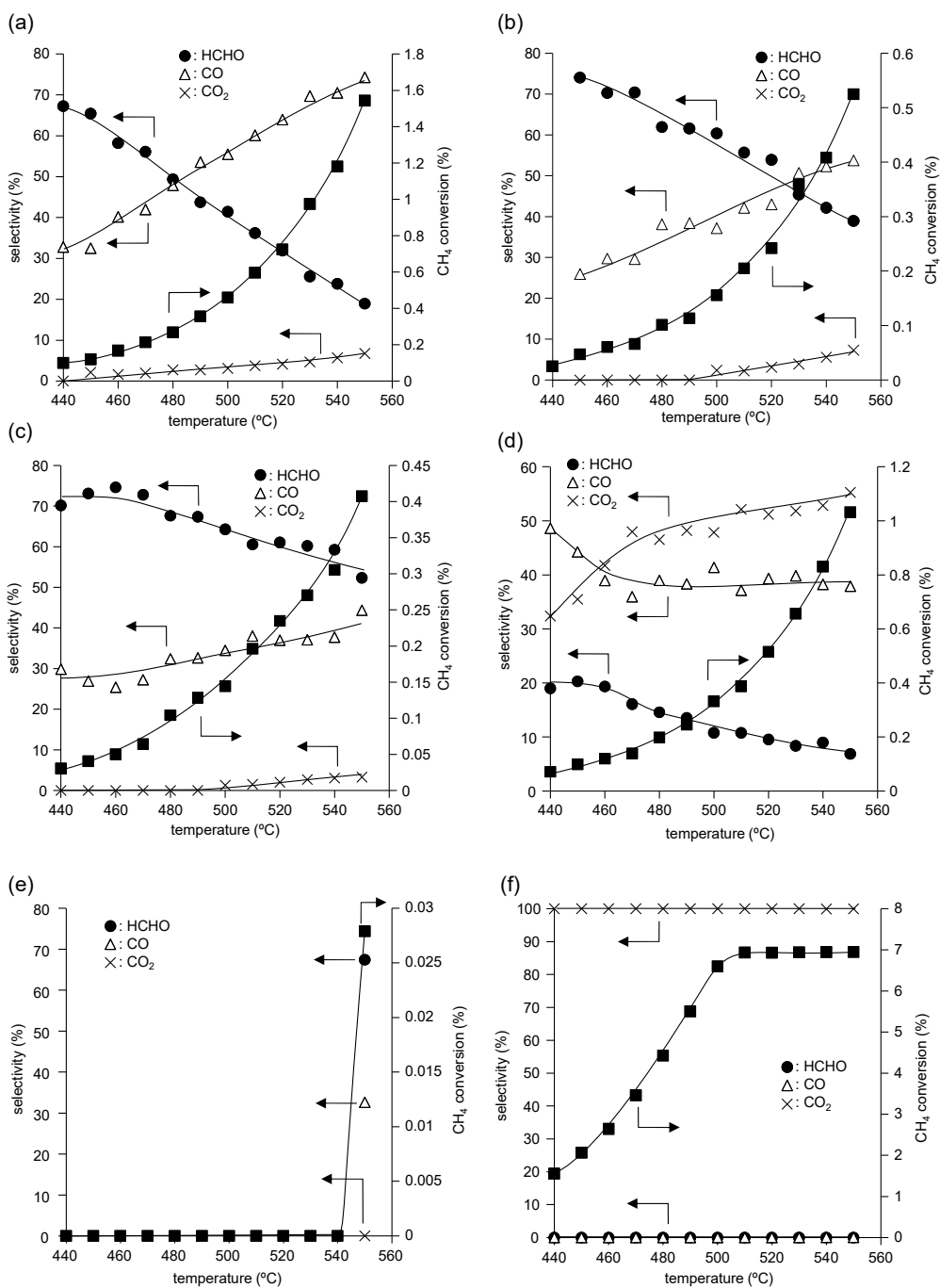
Fig. S7 CH$_4$ conversion and product selectivity as function of reaction temperature for oxidation of CH$_4$ with O$_2$ over (a) FePO$_4$-MA, (b) FePO$_4$-CM-550, (c) FePO$_4$-CM-600, (d) Fe$_3$O$_3$(PO$_4$), (e) Fe$_4$(P$_2$O$_7$)$_3$, and (f) Fe$_2$O$_3$ catalysts.   Reaction conditions: catalyst (50 mg), CH$_4$/O$_2$/N$_2$ (7/1/8 sccm), 440–550 °C.

(a)

after reaction

fresh

10 20 30 40 50 60 70 80
2theta (degree)

(b)

after reaction

fresh

10 20 30 40 50 60 70 80
2theta (degree)

(c)

after reaction

fresh

10 20 30 40 50 60 70 80
2theta (degree)

(d)

after reaction

fresh

10 20 30 40 50 60 70 80
2theta (degree)

(e)

after reaction

fresh

10 20 30 40 50 60 70 80
2theta (degree)

(f)

after reaction

fresh

10 20 30 40 50 60 70 80
2theta (degree)
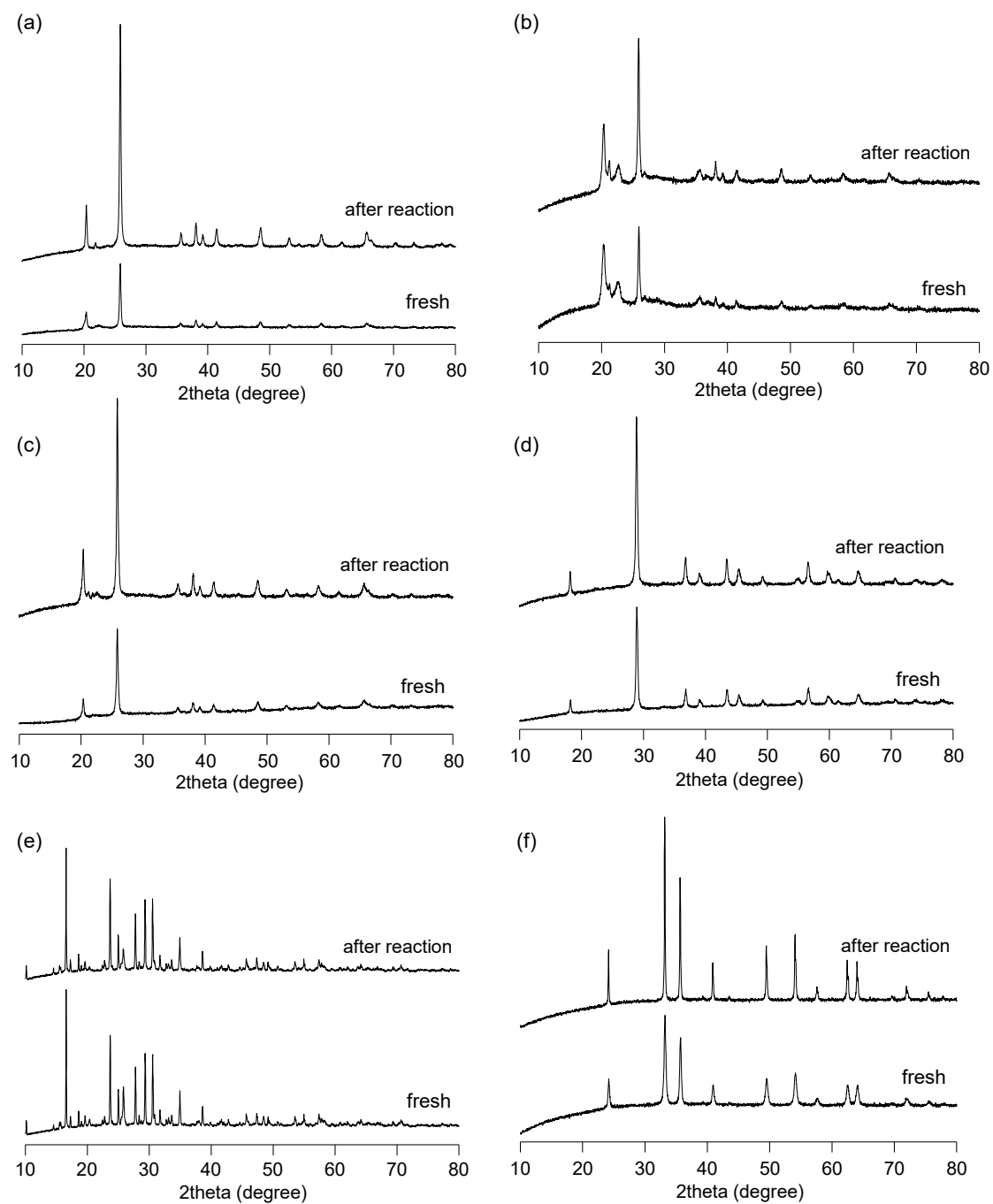
Fig. S8 XRD patterns for fresh and recovered catalysts after oxidation of CH_4 under same conditions as those in Fig. S6; (a) FePO$_4$-MA, (b) FePO$_4$-CM-550, (c) FePO$_4$-CM-600, (d) Fe$_3$O$_3$(PO$_4$), (e) Fe$_4$(P$_2$O$_7$)$_3$, and (f) Fe$_2$O$_3$.
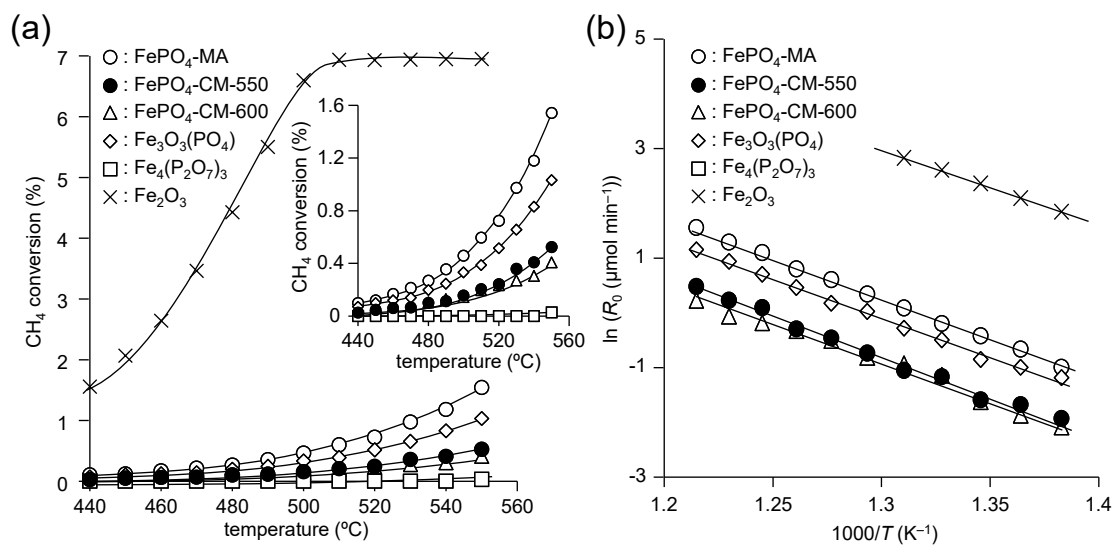
Fig. S9 (a) CH_4 conversion as function of reaction temperature and (b) Arrhenius plots for oxidation of methane over $FePO_4$-MA, $FePO_4$-CM-550, $FePO_4$-CM-600, $Fe_3O_3(PO_4)$, $Fe_4(P_2O_7)_3$, Fe_2O_3 catalysts.   Inset for (a): data for iron phosphate catalysts in CH_4 conversion region of 0–1.6%.   Reaction conditions: catalyst (50 mg), $CH_4/O_2/N_2$ (7/1/8 sccm), 440–550 °C. R_0 values were determined by CH_4 conversion.
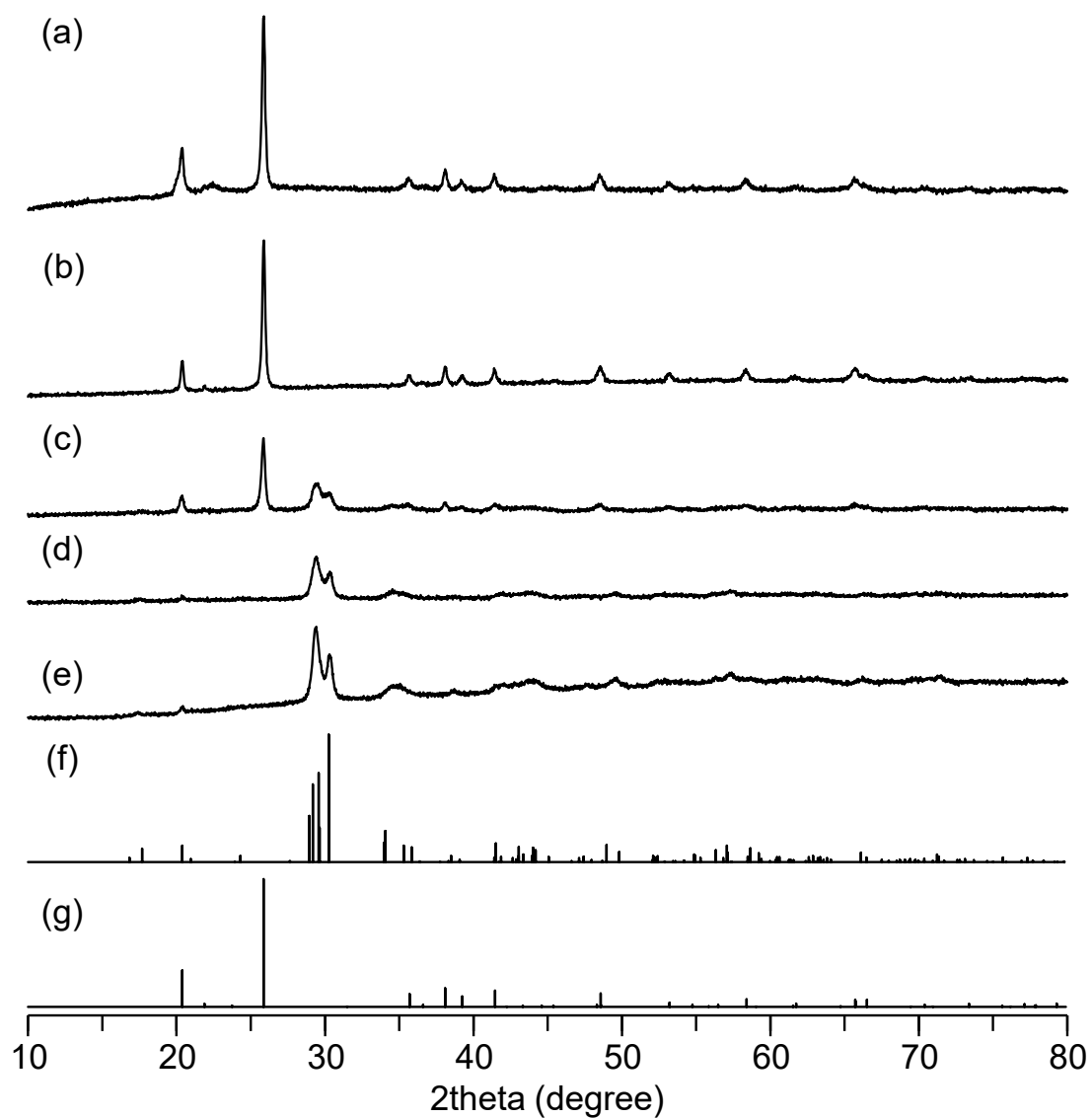
Fig. S10 XRD patterns for (a) fresh $FePO_4$-MA, and $FePO_4$-MA reduced with H_2 at (b) 500, (c) 550, (d) 600, and (e) 650 °C, (f) $Fe_2P_2O_7$ (ICSD 36208), and (g) $FePO_4$ (ICSD 201795). Reduction of the samples was performed in a TG-DTA furnace under the conditions given in Fig. S1(a).
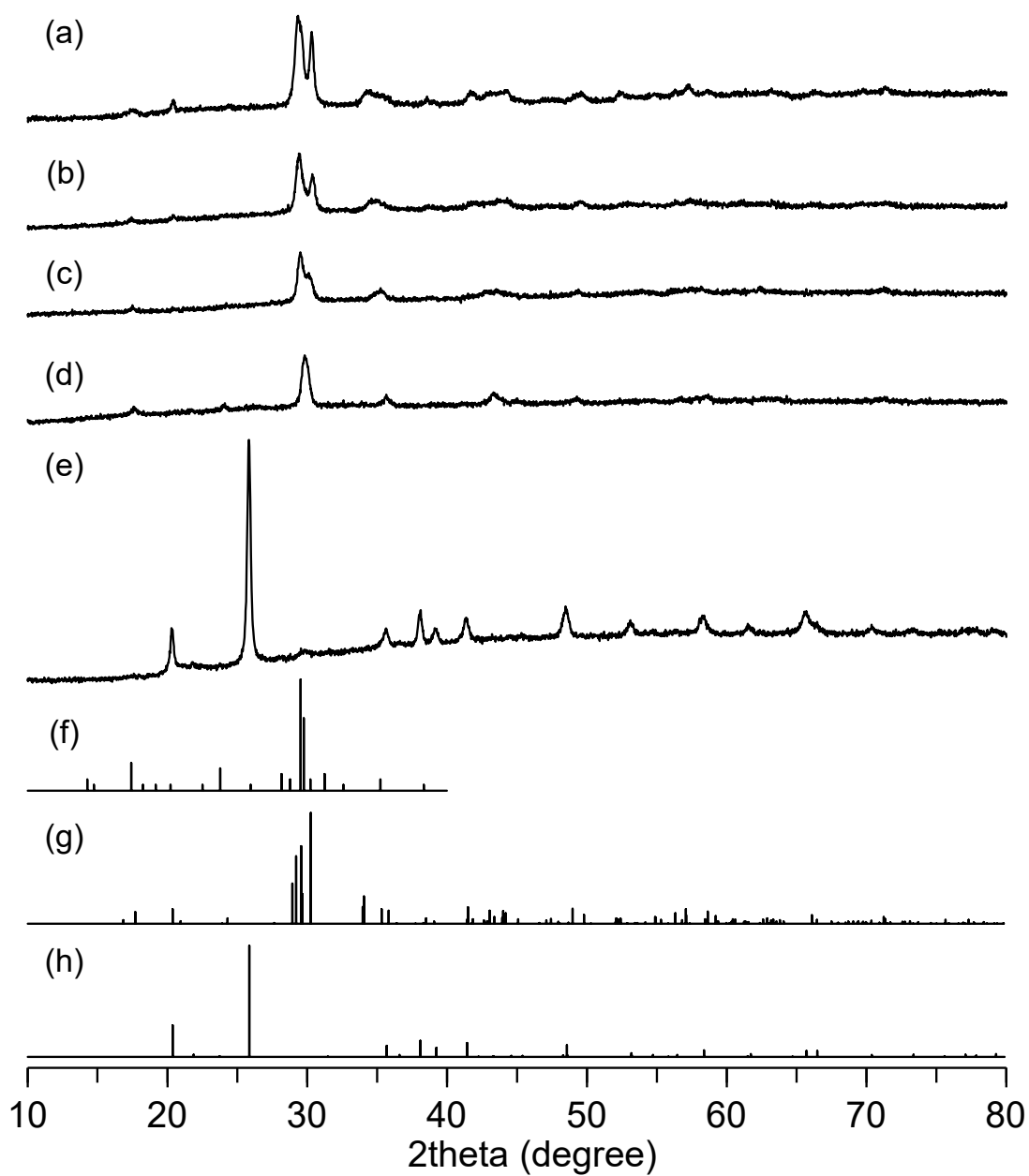
Fig. S11 XRD patterns for (a) fresh $Fe_2P_2O_7$ (prepared by reduction of $FePO_4$-MA), and $Fe_2P_2O_7$ reoxidized with O_2 at (b) 300, (c) 400, (d) 500, and (e) 650 °C, (f) α-$Fe_3(P_2O_7)_2$ (detailed data are shown in Refs. S8 and S9), (g) $Fe_2P_2O_7$ (ICSD 36208), and (h) $FePO_4$ (ICSD 201795). Reoxidation of the samples was performed in a TG-DTA furnace under the conditions given in Fig. S1(b).
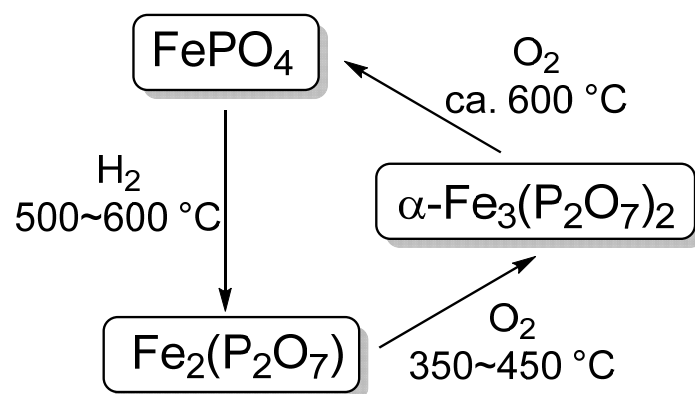
Fig. S12 Possible reaction pathways for redox cycle between $FePO_4$ and $Fe_2P_2O_7$.
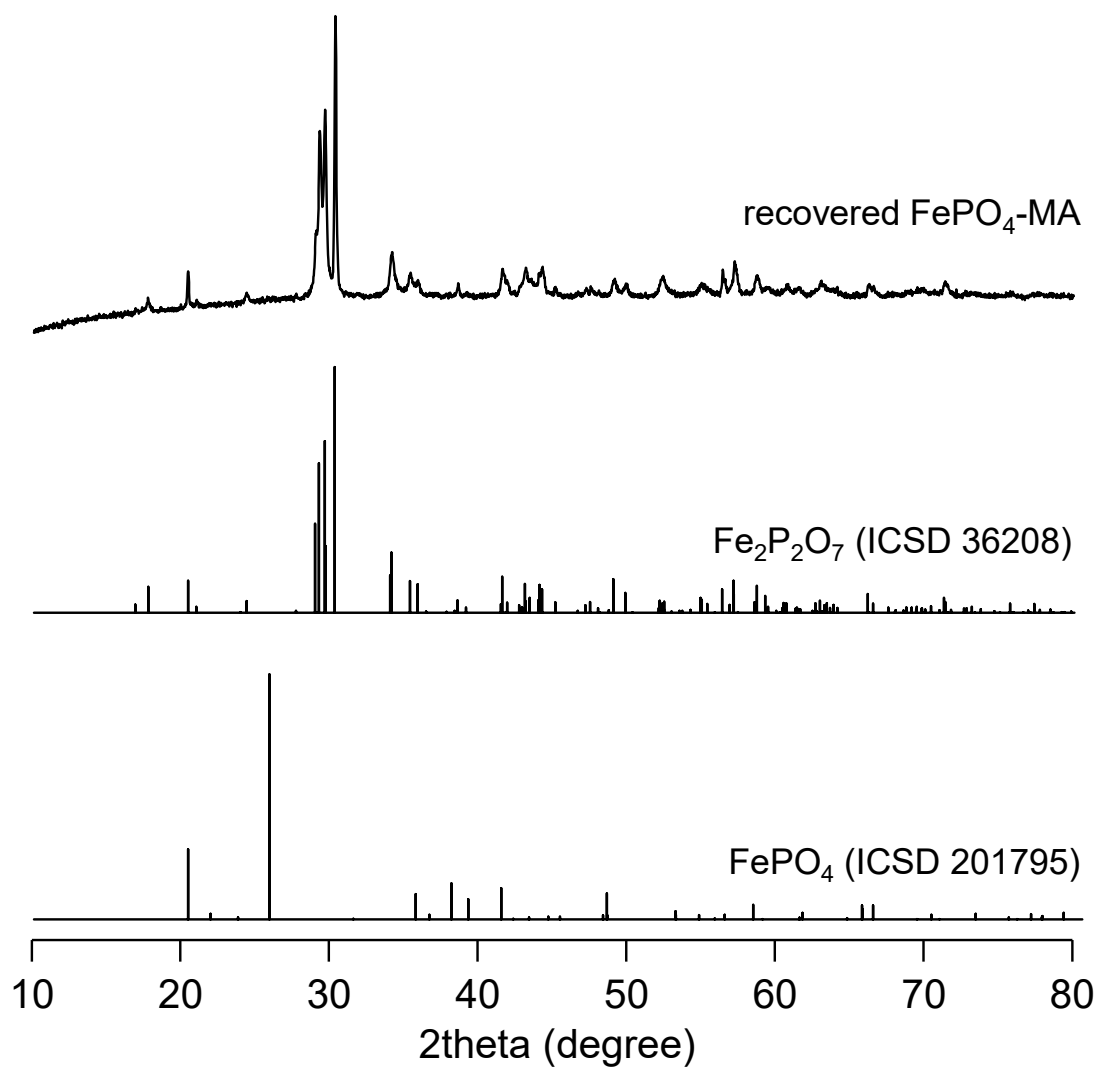
Fig. S13 XRD patterns for recovered FePO4-MA after temperature-programmed reaction measurement as shown in Fig. 6, Fe₂P₂O₇ (ICSD 36208), and FePO₄ (ICSD 201795).
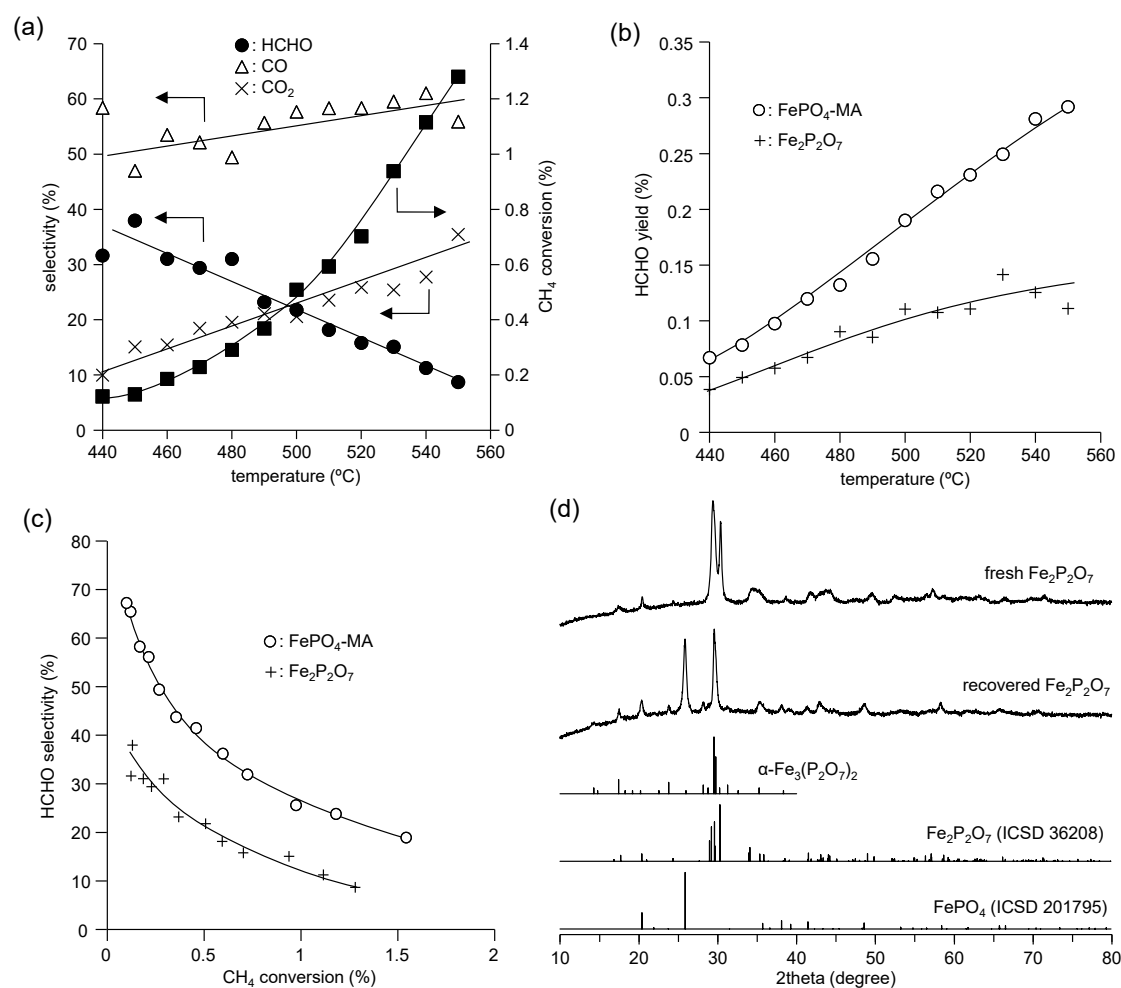
Fig. S14 (a) CH$_4$ conversion, product selectivity, and (b) HCHO yield as function of reaction temperature, and (c) selectivity to HCHO as function of CH$_4$ conversion for oxidation of methane with O$_2$ over Fe$_2$P$_2$O$_7$. Reaction conditions: catalyst (50 mg), CH$_4$/O$_2$/N$_2$ (7/1/8 sccm), 440–550 °C. (d) XRD patterns for fresh Fe$_2$P$_2$O$_7$, recovered Fe$_2$P$_2$O$_7$ after oxidation, α-Fe$_3$(P$_2$O$_7$)$_2$ (detailed data are shown in Refs. S8 and S9), Fe$_2$P$_2$O$_7$ (ICSD 36208), and FePO$_4$ (ICSD 201795).
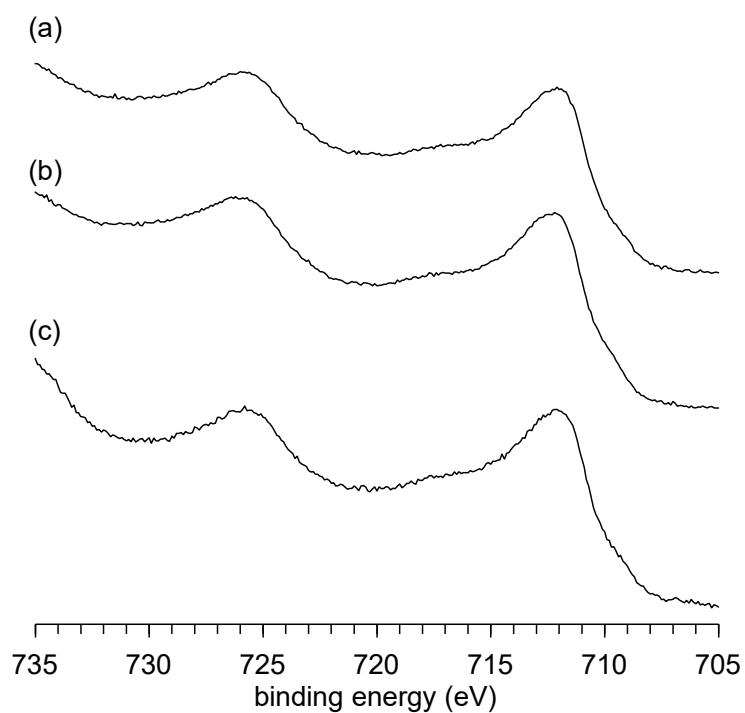
S17

Fig. S15 XPS Fe 2p spectra for (a) fresh FePO$_4$-MA, (b) recovered FePO$_4$-MA after oxidation of CH$_4$ under conditions given in Fig. S7, and (c) recovered FePO$_4$-MA after pulse reaction experiments under conditions given in Fig. 8(a).
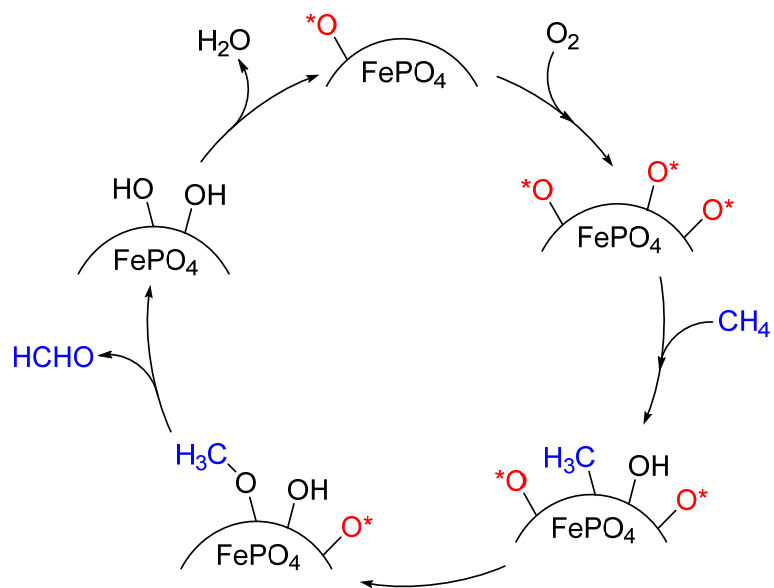
Fig. S16 Proposed reaction mechanism for oxidation of CH_4 with O_2 over $FePO_4$ catalyst reported in Refs. S10 and S11. O*: lattice oxygen atoms in surface region.
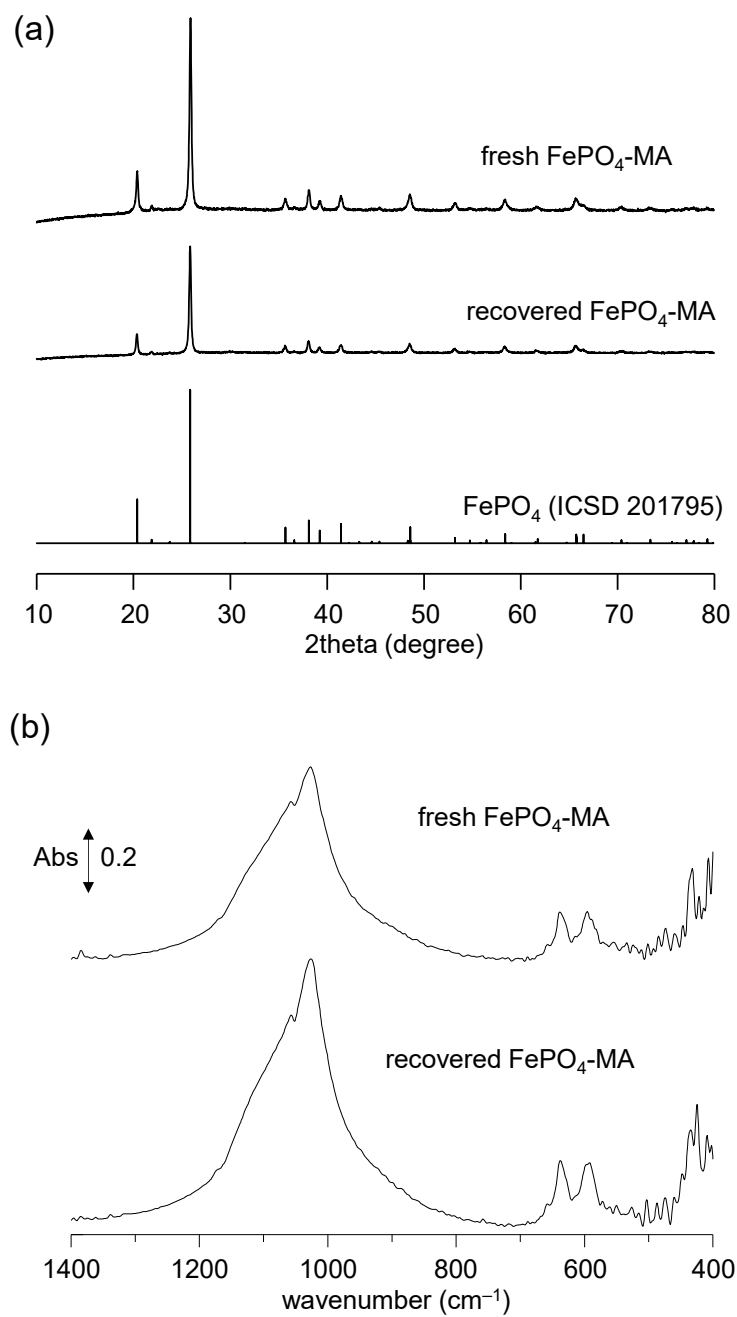
Fig. S17 (a) XRD patterns and (b) IR spectra for fresh and recovered FePO4-MA after pulse-experiments as shown in Fig. 8.
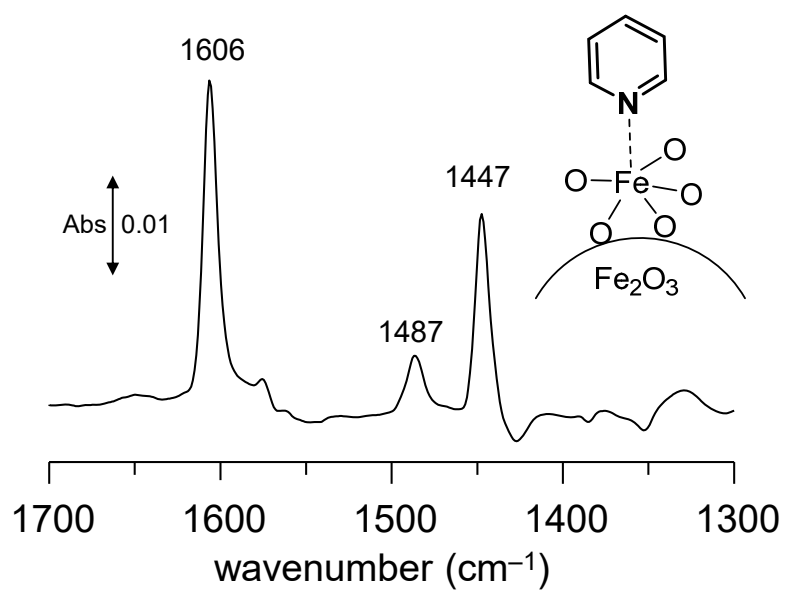
Fig. S18 Difference IR spectra for pyridine-adsorbed Fe_2O_3 at 25 °C.

References

(S1) Y. Yamaguchi, R. Aono, E. Hayashi, K. Kamata and M. Hara, *ACS Appl. Mater. Interfaces*, 2020, **12**, 36004–36013.

(S2) E. Hayashi, Y. Yamaguchi, K. Kamata, N. Tsunoda, Y. Kumagai, F. Oba and M. Hara, *J. Am. Chem. Soc.*, 2019, **141**, 890–900.

(S3) K. Kamata, K. Sugahara, Y. Kato, S. Muratsugu, Y. Kumagai, F. Oba, M. Hara, *ACS Appl. Mater. Interfaces*, 2018, **10**, 23792–23801.

(S4) K. Sugahara, K. Kamata, S. Muratsugu and M. Hara, *ACS Omega*, 2017, **2**, 1608–1616.

(S5) S. Kanai, I. Nagahara, Y. Kita, K. Kamata and M. Hara, *Chem. Sci.*, 2017, **8**, 3146–3153.

(S6) T. Komanoya, K. Nakajima, M. Kitano and M. Hara, *J. Phys. Chem. C*, 2015, **119**, 26540–26546.

(S7) K. Nakajima, Y. Baba, R. Noma, M. Kitano, J. N. Kondo, S. Hayashi and M. Hara, *J. Am. Chem. Soc.*, 2011, **133**, 4224–4227.

(S8) J.-M. M. Millet, *Catal. Rev. - Sci. Eng.*, 1998, **40**, 1–38.

(S9) J.-M. M. Millet, J. C. Vedrine, G. Hecquet, *Stud. Surf. Sci. Catal.*, 1990, **55**, 833–841.

(S10) Y. Wang and K. Otsuka, *J. Catal.*, 1995, **155**, 256–267.

(S11) Y. Wang, X. Wang, Z. Su, Q. Guo, Q. Tang, Q. Zhang and H. Wan, *Catal. Today*, 2004, **93-95**, 155–161.